



Assessing the capability of different satellite observing configurations to resolve the distribution of methane emissions at kilometer scales

Alexander J. Turner^{1,2}, Daniel J. Jacob², Joshua Benmergui², Jeremy Brandman³, Laurent White³, and Cynthia A. Randles³

¹College of Chemistry/Department of Earth and Planetary Sciences, University of California, Berkeley, CA, USA.

²School of Engineering and Applied Sciences, Harvard University, Cambridge, Massachusetts, USA.

³ExxonMobil Research and Engineering Company, Annandale, NJ, USA.

Correspondence to: Alexander J. Turner
(alexjturner@berkeley.edu)

1 **Abstract.** Anthropogenic methane emissions originate from a large number of fine-scale and of-
2 ten transient point sources. Satellite observations of atmospheric methane columns are an attractive
3 approach for monitoring these emissions but have limitations from instrument precision, pixel reso-
4 lution, and measurement frequency. Dense observations will soon be available in both low Earth and
5 geostationary orbits, but the extent to which they can provide fine-scale information on methane
6 sources has yet to be explored. Here we present an observation system simulation experiment
7 (OSSE) to assess the capabilities of different satellite observing system configurations. We conduct a
8 1-week WRF-STILT simulation to generate methane column footprints at $1.3 \times 1.3 \text{ km}^2$ spatial reso-
9 lution and hourly temporal resolution over a $290 \times 235 \text{ km}^2$ domain in the Barnett Shale in Northeast
10 Texas, a major oil/gas field with a large number of point sources. We sub-sample these footprints
11 to match the observing characteristics of the recently launched TROPOMI instrument ($7 \times 7 \text{ km}^2$
12 pixels, 11 ppb precision, daily frequency), the planned GeoCARB instrument ($2.7 \times 3.0 \text{ km}^2$ pixels,
13 4 ppb precision, nominal twice-daily frequency), and other proposed observing configurations. The
14 information content of the various observing systems is evaluated using the Fisher information ma-
15 trix and its eigenvalues. We find that a week of TROPOMI observations should effectively provide
16 regional ($\sim 100 \text{ km}$) information on temporally invariant emissions but is very limited at finer scales.
17 GeoCARB should provide 4-37% of the total information available for temporally invariant emis-
18 sions in the Barnett Shale (~ 100 pieces of information). Improvements to the instrument precision
19 yield greater increases in information content, compared to improved sampling frequency. A preci-
20 sion better than 6 ppb is an important threshold for achieving fine resolution of emissions. Transient



21 emissions would be missed with either TROPOMI or GeoCARB. An aspirational high-resolution
22 geostationary instrument with $1.3 \times 1.3 \text{ km}^2$ pixel resolution, hourly return time, and 1 ppb precision
23 would effectively constrain the temporally invariant emissions in the Barnett Shale at the kilometer
24 scale and provide some information on transient sources.

25 1 Introduction

26 Methane is a greenhouse gas emitted by a range of natural and anthropogenic sources (Kirschke
27 et al., 2013; Saunio et al., 2016; Turner et al., 2017). Anthropogenic methane emissions are difficult
28 to quantify because they tend to originate from a large number of potentially transient point sources
29 such as livestock operations, oil/gas leaks, landfills, and coal mine ventilation. Atmospheric methane
30 observations from surface and aircraft have been used to quantify emissions (e.g., Miller et al., 2013;
31 Caulton et al., 2014; Karion et al., 2013, 2015; Lavoie et al., 2015; Conley et al., 2016; Peischl et al.,
32 2015, 2016; Houweling et al., 2016) but are limited in spatial and temporal coverage. Satellite
33 measurements have dense and continuous coverage but limitations from observational errors and
34 pixel resolution need to be understood. Here we perform an observing system simulation experiment
35 (OSSE) to investigate the information content of different configurations of satellite instruments for
36 observing fine-scale and transient methane sources, taking as a test case the oil/gas production sector.

37 Low-Earth orbit satellite observations of methane by solar backscatter in the shortwave infrared
38 (SWIR) have been available since 2003 from the SCIAMACHY instrument (2003–2012; Franken-
39 berg et al., 2005) and from the GOSAT instrument (2009–present; Kuze et al., 2009, 2016). SWIR
40 instruments measure the atmospheric column of methane with near-unit sensitivity throughout the
41 troposphere. SCIAMACHY and GOSAT demonstrated the capability for high-precision ($<1\%$)
42 measurements of methane from space (Buchwitz et al., 2015), but SCIAMACHY had coarse pix-
43 els ($30 \times 60 \text{ km}^2$ in nadir) and GOSAT has sparse coverage (10-km diameter pixels separated by
44 250 km). Inverse analyses have used observations from these satellite-based instruments to estimate
45 methane emissions at $\sim 100\text{--}1000 \text{ km}$ spatial resolution (e.g., Bergamaschi et al., 2009, 2013; Fraser
46 et al., 2013; Monteil et al., 2013; Wecht et al., 2014a; Cressot et al., 2014; Kort et al., 2014; Turner
47 et al., 2015, 2016a; Alexe et al., 2015; Tan et al., 2016; Buchwitz et al., 2017; Sheng et al., 2017,
48 2018). But such coarse resolution makes it difficult to resolve individual source types because of
49 spatial overlap (Maasackers et al., 2016).

50 Improved observations of methane from space are expected in the near future (Jacob et al., 2016).
51 The GHGSat instrument launched in June 2016 (<http://www.ghgsat.com/>) has $50 \times 50 \text{ m}^2$ effective
52 pixel resolution over selected $12 \times 12 \text{ km}^2$ viewing scenes with a return time of a few weeks, suitable
53 for detecting large point sources. The TROPOMI instrument (Veefkind et al., 2012; Butz et al., 2012;
54 Hu et al., 2016), launched in October 2017, will provide global mapping at $7 \times 7 \text{ km}^2$ nadir resolution
55 once per day. The GeoCARB geostationary instrument (Polonsky et al., 2014; O'Brien et al., 2016)



56 will be launched in the early 2020s with current design values of $3 \times 3 \text{ km}^2$ pixel resolution and
57 twice-daily return time. Additional instruments are presently in the proposal stage with improved
58 combinations of pixel resolution, return time, and instrument precision (Fishman et al., 2012; Butz
59 et al., 2015; Xi et al., 2015).

60 An OSSE simulates the atmosphere as it would be observed by an instrument with a given ob-
61 serving configuration and error specification. Several OSSEs have been conducted to evaluate the
62 potential of satellite observations to quantify methane sources, but they have either been conducted
63 at coarse ($\sim 50 \times 50 \text{ km}^2$) spatial resolution (Wecht et al., 2014b; Bousserez et al., 2016) or assumed
64 idealized flow conditions (Bovensmann et al., 2010; Rayner et al., 2014). Jacob et al. (2016) pre-
65 sented a simple mass balance equation to compare the source detection capabilities of satellite in-
66 struments with different pixel resolutions, precisions, and return times, but they used information
67 from the source pixel only and assumed a homogeneous flow. Here we use a 1-week simulation of
68 atmospheric methane with $1.3 \times 1.3 \text{ km}^2$ resolution over a $290 \times 235 \text{ km}^2$ domain to simulate con-
69 tinuous and transient emissions in the Barnett Shale region of Northeast Texas, and from there we
70 quantify the capability of different satellite instrument configurations to resolve and quantify these
71 sources at the kilometer scale.

72 2 High-resolution OSSE environment

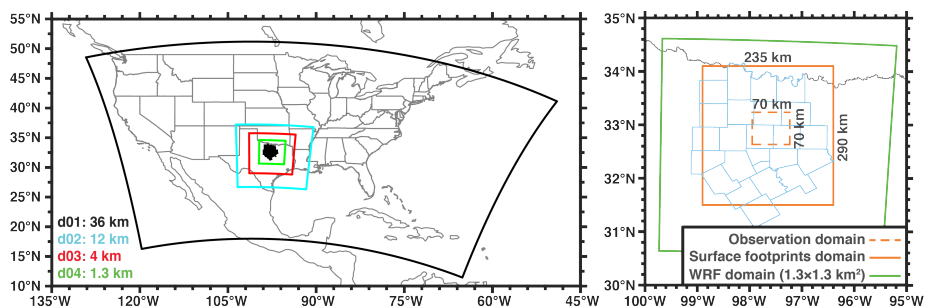


Fig. 1. High-resolution OSSE domain. Left panel shows the successive nested WRF domains at 36, 12, 4, and 1.3 km spatial resolutions, with the coarser domains providing initial and boundary conditions for the finer domains. Black shaded region is the Barnett Shale region of Northeast Texas. Right panel shows the domain for the OSSE. Green box is the innermost 1.3 km WRF domain, dashed orange box is the observation domain, solid orange box is the domain over which the footprints are computed. Light blue lines indicate the counties in the Barnett Shale.

73 We simulate atmospheric methane concentrations over the Barnett Shale of Northeast Texas at
74 $1.3 \times 1.3 \text{ km}^2$ horizontal resolution for the period of October 19-25, 2013 using a framework sim-
75 ilar to that of Turner et al. (2016b). The simulation uses version 3.5 of the Weather Research



76 and Forecasting (WRF) model (Skamarock et al., 2008) over a succession of nested domains (left
77 panel in Figure 1) with $1.3 \times 1.3 \text{ km}^2$ spatial resolution in the innermost domain covering 290×235
78 km^2 . There are 50 vertical layers up to 100 hPa. Boundary-layer physics are represented with the
79 Mellor-Yamada-Janic scheme and the land surface is represented with the 5-layer slab model (Ska-
80 marock et al., 2008). The simulation is initialized with assimilated meteorological observations
81 from the North American Regional Reanalysis ([https://www.ncdc.noaa.gov/data-access/model-data/](https://www.ncdc.noaa.gov/data-access/model-data/model-datasets/north-american-regional-reanalysis-narr)
82 [model-datasets/north-american-regional-reanalysis-narr](https://www.ncdc.noaa.gov/data-access/model-data/model-datasets/north-american-regional-reanalysis-narr)). Overlapping 30-hour forecasts were ini-
83 tialized every 24 hours at 00 UTC and the first 6 hours of each forecast were discarded to allow for
84 model spinup. Grid nudging was used in the outer-most domain.

85 WRF meteorology is used to drive the Stochastic Time-Inverted Lagrangian Transport (STILT)
86 model (Lin et al., 2003). STILT is a Lagrangian particle dispersion model. It advects an ensemble
87 of particles backward in time from selected receptor locations, using the archived hourly WRF wind
88 fields and boundary-layer heights. STILT calculates the footprint for the receptors; a spatio-temporal
89 map of the sensitivity of observations to emissions contributing to the concentration at each selected
90 receptor location and time. We use STILT to calculate 10-day footprints for hourly column concen-
91 trations at $1.3 \times 1.3 \text{ km}^2$ resolution over a $70 \times 70 \text{ km}^2$ domain in the innermost WRF nest, tracking
92 the resulting footprints over a $290 \times 235 \text{ km}^2$ domain (right panel in Figure 1). With this system we
93 examine the constraints on emissions over the $290 \times 235 \text{ km}^2$ domain provided by dense SWIR satel-
94 lite observations (over the $70 \times 70 \text{ km}^2$ domain) that have up to 1.3 km pixel resolution and hourly
95 daytime frequency. Footprints for each column are obtained by releasing 100 STILT particles from
96 vertical levels centered at 28 m above the surface, 97 m, 190 m, 300 m, and 8 additional levels up
97 to 14 km altitude spaced evenly on a pressure grid. The column footprints are then constructed by
98 summing the pressure-weighted contributions from individual levels, using a typical SWIR averag-
99 ing kernel taken from Worden et al. (2015) with near-uniformity in the troposphere, and correcting
100 for water vapor (see Appendix A in O'Dell et al., 2012).

101 The footprint for the i^{th} receptor location and time can be expressed as a vector $\mathbf{h}_i = (\partial y_i / \partial \mathbf{x})^T$
102 describing the sensitivity of the column concentration y at that receptor location and time to the
103 emission fluxes \mathbf{x} over the $290 \times 235 \text{ km}^2$ domain and previous times extending up to 10 days. Here
104 \mathbf{x} is arranged as a vector of length n assembling all the emission grid cells and hours, allowing the
105 emissions to vary on an hourly basis. The column concentration is expressed as the dry air column-
106 average mixing ratio (ppb) following common practice (Jacob et al., 2016). The emissions \mathbf{x} have
107 units of $\text{nmol m}^{-2} \text{ s}^{-1}$, so that the footprint has units of $\text{ppb nmol}^{-1} \text{ m}^2 \text{ s}$. The column concentration
108 for the i^{th} observation (y_i) can be reconstructed from its footprint as:

$$y_i = \mathbf{h}_i \mathbf{x} + b_i \quad (1)$$

109 where b_i is the background column concentration upwind of the $290 \times 235 \text{ km}^2$ domain. We can
110 then write the full set of observations as a vector \mathbf{y} of length m , and reshape the set of m footprint



111 vectors \mathbf{h} into an $m \times n$ sparse matrix $\mathbf{H} = \partial \mathbf{y} / \partial \mathbf{x}$ (where m is the number of observations and n is
112 the number of state vector elements):

$$\mathbf{y} = \mathbf{H}\mathbf{x} + \mathbf{b} \quad (2)$$

113 where \mathbf{b} is the background vector with elements b_i and \mathbf{H} is the Jacobian matrix that maps emissions
114 to concentration enhancements due to emissions within our domain.

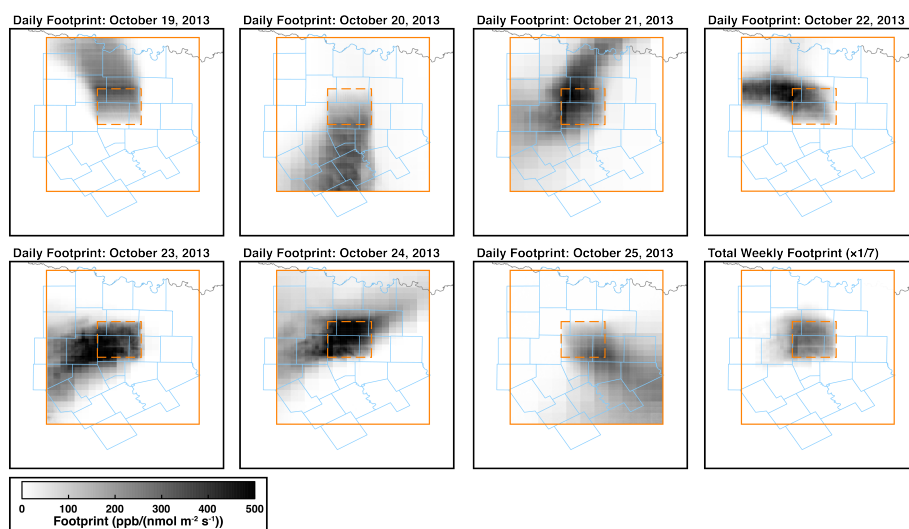


Fig. 2. Summed methane column footprints for all $1.3 \times 1.3 \text{ km}^2$ grid cells in the $70 \times 70 \text{ km}^2$ observation domain defined by the dashed orange box. The footprints are calculated from 8 to 17 local time over the $290 \times 235 \text{ km}^2$ domain defined by the solid orange box. Bottom right panel shows the summed footprint for the full week, scaled by $1/7$.

115 Figure 2 shows the sum of all column footprints produced on individual days for the $70 \times 70 \text{ km}^2$
116 observation domain. The footprints show large variability from day to day over the course of the
117 week, reflecting meteorological variability. For example, winds are from the north on October 19th
118 and from the south on October 20th. The winds are weak on October 24th, resulting in a strong
119 local contribution to the footprint. Summing the footprints over the course of the week (bottom right
120 panel of Fig. 2), we find that the observations are strongly sensitive to the core $70 \times 70 \text{ km}^2$ domain
121 with a diffuse sensitivity over the outer $290 \times 235 \text{ km}^2$ domain.

122 The footprint information can be combined with an emission inventory for the $290 \times 235 \text{ km}^2$
123 domain to generate a field of column concentrations over the $70 \times 70 \text{ km}^2$ domain as would be ob-
124 served from satellite. We use for this purpose the Environmental Defense Fund (EDF) inventory for
125 the Barnett Shale in October 2013 at $4 \times 4 \text{ km}^2$ resolution compiled by Lyon et al. (2015). We down-
126 scale the EDF inventory by uniform attribution from $4 \times 4 \text{ km}^2$ to $1.3 \times 1.3 \text{ km}^2$ spatial resolution.

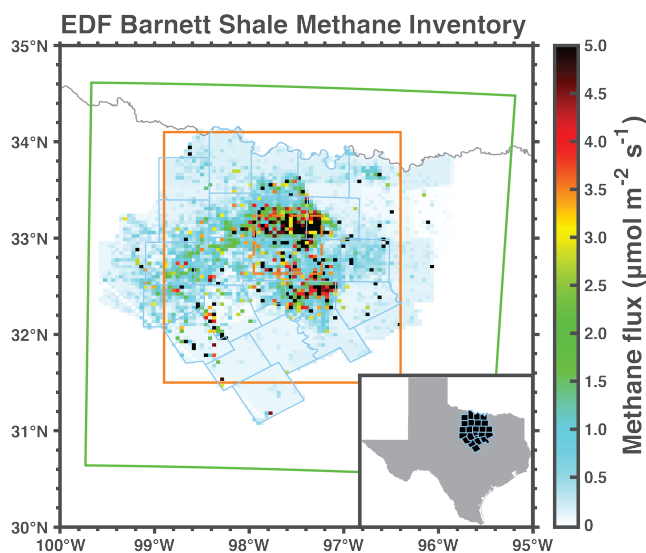


Fig. 3. Gridded Environmental Defense Fund (EDF) methane emission inventory for the Barnett Shale in Northeast Texas in October 2013 (Lyon et al., 2015). Spatial resolution is $4 \times 4 \text{ km}^2$. White areas are outside the inventory domain.

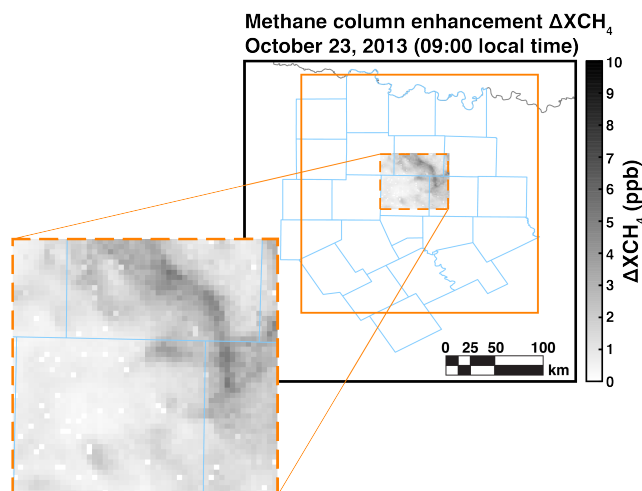


Fig. 4. Simulated methane concentration enhancements relative to background ($\Delta X\text{CH}_4 = \mathbf{Hx}$) in the $70 \times 70 \text{ km}^2$ observation domain of the Barnett Shale (dashed orange box), as derived from the downscaled EDF methane inventory (\mathbf{x}) and the WRF-STILT footprints (\mathbf{H}) within the $290 \times 235 \text{ km}^2$ OSSE domain (solid orange box). Values are for October 23 at 9 local time.



Table 1. Satellite observing systems considered in this work.

Instrument	Observation Frequency ^a	Pixel resolution (km ²)	Precision (ppb)
hi-res ^b	hourly	1.3 × 1.3	1.0
GeoCARB (hourly)	hourly	2.7 × 3.0	4.0
GeoCARB	twice daily	2.7 × 3.0	4.0
GeoCARB (daily)	daily	2.7 × 3.0	4.0
TROPOMI	daily	7.0 × 7.0	10.8

^aHourly observations are 10 times per day at 8-17 local time, twice daily observations are at 10 and 14 local time, and daily observations are at 13 local time.

^bAspirational instrument with the highest observation frequency and pixel resolution that can be simulated within our OSSE framework.

127 The inventory is shown in Fig. 3 and includes contributions from oil/gas production, livestock op-
128 erations, landfills, and urban emissions from the Dallas-Fort Worth area. It provides mean monthly
129 values with no temporal resolution, but presumes that some sources will behave as sporadic large
130 transients (Zavala-Araiza et al., 2015). Figure 4 shows an example of the methane column enhance-
131 ments above background (**Hx**) computed at 9 local time on October 23. We find enhancements
132 in the range of 0-10 ppb due to emissions within the 290×235 km² OSSE footprint domain. In
133 what follows we will examine the potential of different satellite observing systems to detect these
134 enhancements relative to the background and interpret them in terms of local sources.

135 3 Information content of different satellite observing systems

136 We aim to determine the information content from different satellite-based observing systems regard-
137 ing the spatial and temporal distribution of emissions in the Barnett Shale. We consider both steady
138 and potentially transient emissions with 5 different satellite observing configurations (Table 1).
139 TROPOMI (global daily mapping, 7×7 km² nadir pixel resolution, 11 ppb precision; Veeffkind et al.,
140 2012) was launched in October 2017 and is expected to provide an operational data stream by the end
141 of 2018. GeoCARB (geostationary, 2.7×3.0 km² pixel resolution, 4 ppb precision; O'Brien et al.,
142 2016) is planned for launch in the early 2020s and its observation schedule is still under discussion
143 with a tentative design for observations twice daily; here we examine different return frequencies of
144 hourly, twice daily, and daily. Finally, the hypothetical “hi-res” configuration assumes geostation-
145 ary hourly observations at the 1.3×1.3 km² pixel resolution of our WRF simulation and with 1 ppb
146 precision; it represents an aspirational system that combines the frequent return time, fine pixel res-
147 olution, and high precision of instruments presently at the proposal stage (Bovensmann et al., 2010;
148 Fishman et al., 2012; Xi et al., 2015). All configurations are filtered for cloudy scenes.



149 The various satellite observing configurations of Table 1 differ in their return frequency, pixel
 150 resolution, and instrument precision. The benefit of improving any of these attributes may be lim-
 151 ited by error in the forward model used in the inverse analysis (i.e., the Jacobian matrix \mathbf{H}) and by
 152 spatial or temporal correlation of the errors. These limitations are described by the model-data mis-
 153 match error covariance matrix (\mathbf{R}) including summed contributions from the instrument, forward
 154 model, and representation errors (Turner and Jacob, 2015; Brasseur and Jacob, 2017). Representa-
 155 tion errors are negligible here because the instrument pixels are commensurate or coarser than
 156 the model grid resolution. Instrument error (i.e., precision) is listed in Table 1. Forward model
 157 error is estimated by computing STILT footprints for a subset of the meteorological period using
 158 the Global Data Assimilation System (GDAS; [https://www.ncdc.noaa.gov/data-access/model-data/](https://www.ncdc.noaa.gov/data-access/model-data/model-datasets/global-data-assimilation-system-gdas)
 159 [model-datasets/global-data-assimilation-system-gdas](https://www.ncdc.noaa.gov/data-access/model-data/model-datasets/global-data-assimilation-system-gdas)), applying the two sets of footprints to either
 160 the EDF methane inventory (Fig. 3; Lyon et al., 2015) or the gridded EPA inventory (Maasakkers
 161 et al., 2016), and computing semivariograms of differences in column concentrations. From this we
 162 obtain a forward model error standard deviation of 4 ppb with an error correlation length scale of 40
 163 km. We assume a temporal model error correlation length of 2 hours. Sheng et al. (2017) previously
 164 derived a temporal model error correlation length of 5 hours in simulation of TCCON methane col-
 165 umn observations at 25 km resolution, and we expect our correlation length to be shorter because of
 166 the finer resolution.

167 Bayesian inference is commonly used when estimating methane emissions with atmospheric ob-
 168 servations, allowing for errors in the observations and in the prior estimates:

$$P(\mathbf{x}|\mathbf{y}) \propto P(\mathbf{y}|\mathbf{x})P(\mathbf{x}) \quad (3)$$

169 where $P(\mathbf{x}|\mathbf{y})$ is the posterior probability density function (pdf) of the state vector (\mathbf{x}) given the
 170 observations (\mathbf{y}), $P(\mathbf{y}|\mathbf{x})$ is the conditional pdf of \mathbf{y} given \mathbf{x} , and $P(\mathbf{x})$ is the prior pdf of \mathbf{x} . A
 171 common assumption is that $P(\mathbf{y}|\mathbf{x})$ and $P(\mathbf{x})$ are normally distributed which allows us to write the
 172 posterior pdf as

$$P(\mathbf{x}|\mathbf{y}) \propto \exp \left\{ -\frac{1}{2}(\mathbf{y} - \mathbf{H}\mathbf{x})^T \mathbf{R}^{-1}(\mathbf{y} - \mathbf{H}\mathbf{x}) - \frac{1}{2}(\mathbf{x} - \mathbf{x}_a)^T \mathbf{B}^{-1}(\mathbf{x} - \mathbf{x}_a) \right\} \quad (4)$$

173 where \mathbf{B} is the $n \times n$ prior error covariance matrix and \mathbf{x}_a is the $n \times 1$ vector of prior fluxes. The
 174 most probable solution is obtained by minimizing the cost function:

$$\mathcal{J}(\mathbf{x}) = \frac{1}{2}(\mathbf{y} - \mathbf{H}\mathbf{x})^T \mathbf{R}^{-1}(\mathbf{y} - \mathbf{H}\mathbf{x}) + \frac{1}{2}(\mathbf{x} - \mathbf{x}_a)^T \mathbf{B}^{-1}(\mathbf{x} - \mathbf{x}_a) \quad (5)$$

175 yielding the posterior estimate ($\hat{\mathbf{x}}$):

$$\hat{\mathbf{x}} = \mathbf{x}_a + \underbrace{(\mathbf{H}^T \mathbf{R}^{-1} \mathbf{H} + \mathbf{B}^{-1})^{-1} \mathbf{H}^T \mathbf{R}^{-1}(\mathbf{y} - \mathbf{H}\mathbf{x})}_{\text{posterior covariance matrix}} \quad (6)$$



Table 2. Cost functions for different formulations of the inverse problem^a.

Method	Cost function
Least-squares regression	$(\mathbf{y} - \mathbf{H}\mathbf{x})^T \mathbf{R}^{-1} (\mathbf{y} - \mathbf{H}\mathbf{x})$
LASSO regression	$(\mathbf{y} - \mathbf{H}\mathbf{x})^T \mathbf{R}^{-1} (\mathbf{y} - \mathbf{H}\mathbf{x}) + \gamma \sum_i x_i $
Tikhonov regularization	$(\mathbf{y} - \mathbf{H}\mathbf{x})^T \mathbf{R}^{-1} (\mathbf{y} - \mathbf{H}\mathbf{x}) + \gamma \mathbf{x}^T \mathbf{x}$
Bayesian inference, Gaussian	$(\mathbf{y} - \mathbf{H}\mathbf{x})^T \mathbf{R}^{-1} (\mathbf{y} - \mathbf{H}\mathbf{x}) + (\mathbf{x} - \mathbf{x}_a)^T \mathbf{B}^{-1} (\mathbf{x} - \mathbf{x}_a)$
Geostatistical inverse model	$(\mathbf{y} - \mathbf{H}\mathbf{x})^T \mathbf{R}^{-1} (\mathbf{y} - \mathbf{H}\mathbf{x}) + (\mathbf{x} - \mathbf{G}\boldsymbol{\beta})^T \mathbf{B}^{-1} (\mathbf{x} - \mathbf{G}\boldsymbol{\beta})$

^a γ is the regularization parameter for LASSO regression and Tikhonov regularization. \mathbf{G} is a matrix with columns corresponding to different spatial datasets and $\boldsymbol{\beta}$ is a vector of drift coefficients for the spatial datasets. Other variables defined in the text.

176 with an $n \times n$ posterior error covariance matrix:

$$\mathbf{Q} = \underbrace{(\mathbf{H}^T \mathbf{R}^{-1} \mathbf{H})}_{\text{observations}} + \underbrace{\mathbf{B}^{-1}}_{\text{prior}} \quad (7)$$

177 that characterizes the uncertainty in the solution. The first term in the posterior covariance ma-
 178 trix is known as the Fisher information matrix: $\mathcal{F} = \mathbf{H}^T \mathbf{R}^{-1} \mathbf{H}$ (see, for example, Rodgers, 2000;
 179 Tarantola, 2004). \mathcal{F} defines the observational contribution to the posterior uncertainty.

180 Comparison between \mathcal{F} and \mathbf{B}^{-1} identifies the extent to which the observations reduce the un-
 181 certainty in the fluxes. Specifically, the number of pieces of information on emissions acquired to
 182 better than measurement error is the number of eigenvalues of $\mathbf{B}^{1/2} \mathcal{F} \mathbf{B}^{1/2}$ that are greater than
 183 unity (Rodgers, 2000). As such, the Fisher information matrix and prior error covariance matrix can
 184 quantify the effective rank of the observing system.

185 A drawback with this formulation of the information content is that it relies on the assumption of
 186 a Gaussian prior pdf. A number of papers have suggested that the pdf of methane emissions from a
 187 given source may be skewed, with a “fat tail” of transient high emissions (e.g., Brandt et al., 2014;
 188 Zavala-Araiza et al., 2015; Frankenberg et al., 2016). Alternate formulations for the cost function
 189 to be minimized may include no prior information (least-squares regression), a prior constraint that
 190 promotes a sparse solution (e.g., Candes and Wakin, 2008), a prior constraint based on frequen-
 191 tist regularization approaches (such as LASSO regression or Tikhonov regularization), or a prior
 192 constraint based on the spatial patterns of emissions rather than their magnitudes (geostatistical in-
 193 version). Table 2 lists the corresponding formulations. From Table 2 we see that the observation term
 194 is the same in all cases. Thus the Fisher information matrix provides a general measure of the in-
 195 formation content provided by an observing system, independent of the form of the prior constraint,
 196 and we use it in what follows as a measure of the information content.

197 The Fisher information matrix is an $n \times n$ matrix. Each of its n eigenvectors represent an inde-
 198 pendent normalized emission flux pattern and the corresponding eigenvalues are the inverses of the
 199 error variances associated with that pattern. A more useful way of stating this is that the inverse



200 square root of the i^{th} eigenvalue of \mathcal{F} represents the flux threshold f_i needed for the observations
201 to be able to constrain the emission flux pattern represented by the i^{th} eigenvector. Whether that
202 flux threshold is useful depends on the magnitude of the emissions, and this can be assessed for the
203 problem at hand. Thus the eigenanalysis of the Fisher information matrix gives us a general estimate
204 of the capability of an observing system to quantify emissions, which can then be applied to any
205 actual $n \times n$ emission field.

206 For a given emission field, we may expect that some of the n emission flux patterns will be
207 usefully constrained by the observing system while others are not. The number of patterns that are
208 usefully constrained represents the number $\mathcal{I} \leq n$ pieces of information on emissions provided by
209 the observing system. We will equivalently refer to it as the rank of the Fisher information matrix.
210 This is determined by comparing the eigenvalues of an emission inventory (e_i) to the flux thresholds.
211 The number of e_i larger than the corresponding f_i provides a cut-off to estimate \mathcal{I} :

$$\mathcal{I} = \sum_i \begin{cases} 1, & e_i > f_i \\ 0, & e_i \leq f_i \end{cases} \quad (8)$$

212 In the case of Bayesian inference, this is roughly equivalent to the degrees of freedom for signal with
213 a diagonal prior error covariance matrix and a relative uncertainty of 100%. But the eigenanalysis
214 of the Fisher information matrix provides a more general approach of the capability of an observ-
215 ing system that can be confronted to any prior constraint and allows intercomparison of different
216 observing system configurations.

217 There is an inconsistency in this formulation of \mathcal{I} : \mathcal{F} and \mathbf{B}^{-1} have different eigenspaces. In this
218 work we have chosen to treat these matrices separately because, in practice, it is computationally
219 infeasible to directly compute the eigenvalues of the matrix product if n is large, as in the case here
220 of constraining hourly emissions of the spatially distributed inventory. This inconsistency results in
221 our estimate of \mathcal{I} likely being an upper bound on the information content (see Appendix for details).

222 4 Comparing different satellite configurations

223 The eigenanalysis of Section 3 allows us to intercompare the value of different satellite configura-
224 tions for resolving the fine-scale patterns of methane emissions within a given domain. Here we
225 apply it to the Barnett Shale domain of Section 2. We consider two limiting cases: Case #1 assumes
226 the emissions to be temporally invariant and Case #2 assumes the emissions to vary hourly with no
227 temporal correlation. In Case #1 the problem is typically overdetermined ($m > n$), depending on
228 the satellite configuration, and the maximum rank of \mathcal{F} is n (the number of emission grid cells). In
229 Case #2 the problem is underdetermined ($m < n$) and the maximum rank of \mathcal{F} is m (the number of
230 observations).

231 In both Case #1 and #2, the observations only provide useful information (as defined by Eq. 8) if
232 the signal is larger than the noise, as diagnosed by the $e_i > f_i$ criterion of Eq. 8. Here the emissions



233 are the downscaled EDF inventory, which includes 40,140 grid cells in the $290 \times 235 \text{ km}^2$ inversion
 234 domain ($n = 40,140$ in Case #1 with temporally invariant emissions) but only 2,601 of those grid
 235 cells are within the $70 \times 70 \text{ km}^2$ observation domain (dashed orange box in Fig. 1) where we might
 236 expect the observations to provide the strongest constraints. In Case #2 with temporally variable
 237 emissions we have $n = 40,140 \times 24 = 963,360$ grid cells for a single day.

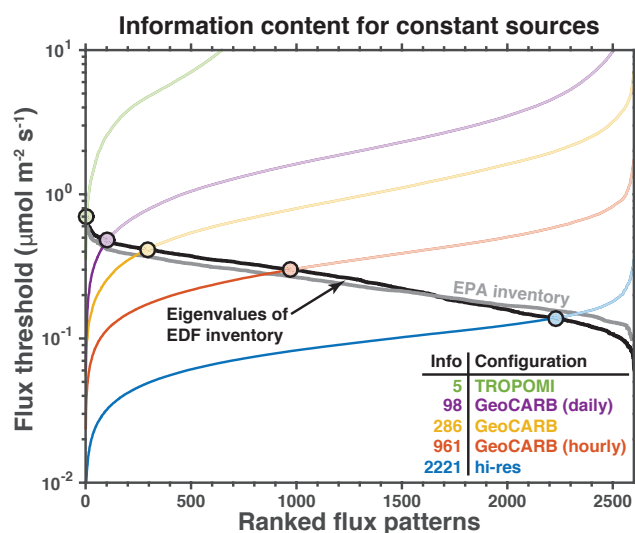


Fig. 5. Capability of different configurations for satellite observations of atmospheric methane (Table 1) to resolve the fine-scale ($1.3 \times 1.3 \text{ km}^2$) patterns of variability of temporally invariant emissions in a $290 \times 235 \text{ km}^2$ domain and for a 1-week observation period. The colored lines show the flux thresholds for the different emission patterns of variability in the domain, as given by the ordered inverse square roots of the eigenvalues of the Fisher information matrix. Solid black line is the eigenvalues of the emissions from the EDF Barnett Shale methane inventory (Lyon et al., 2015) and the solid gray line is the gridded EPA inventory. The region above the black line is where the noise is larger than the signal. Filled circles indicate the information content of the observing system (\mathcal{I}) for a given satellite configuration at $1.3 \times 1.3 \text{ km}^2$ spatial resolution. Inset table lists the information contents for the five configurations.

238 Figure 5 shows the ensemble of flux thresholds for the five satellite configurations, assuming
 239 temporally invariant emissions. The ranked flux patterns are on the abscissa; leading flux patterns
 240 correspond to larger patterns of variability (e.g., regional-scale emissions), and the trailing flux pat-
 241 terns correspond to fine-scale variability. The corresponding flux thresholds are on the ordinate.
 242 The flux threshold is lowest for the leading flux patterns and largest for the trailing flux patterns.
 243 This means that the regional-scale emissions are easiest to quantify and the finer-scale emissions are
 244 increasingly difficult to quantify. The information content (\mathcal{I}) is obtained from the intersection of
 245 the flux thresholds (colored lines) with the eigenvalues from the emission inventory (black line). A

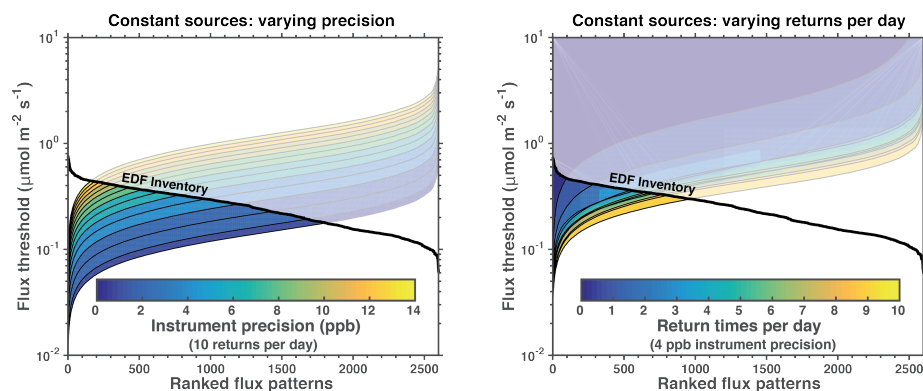


Fig. 6. Capability of GeoCARB-like satellite configurations to resolve the fine-scale ($1.3 \times 1.3 \text{ km}^2$) patterns of variability of temporally invariant emissions in a $290 \times 235 \text{ km}^2$ domain and for a 1-week observation period. Left panel shows the results for a configuration with 10 returns per day (hourly observations) where the instrument precision is varied from 0 to 14 ppb. Right panel shows the results for a configuration with 4 ppb instrument precision and the return frequency per day is varied from 1 to 10. Solid black line shows eigenvalues of the EDF Barnett Shale methane emission inventory (Lyon et al., 2015). The region above the black line is where the noise is larger than the signal.

246 higher information content means that finer scales of emission variability can be detected.

247 From Fig. 5, we see that a week of TROPOMI observations provides 5 pieces of information,
248 indicating that TROPOMI should be able to constrain the mean emissions from the Barnett Shale
249 and the coarse spatial distribution of these emissions. The three GeoCARB configurations provide
250 98–961 pieces of information dependent on whether the observations are daily, twice daily, or hourly.
251 Hourly observations provide 10 times more information (as defined by Eq. 8) on emission patterns
252 than daily observations, and 3 times more than twice-daily observations (the default configuration
253 of GeoCARB). Remarkably, more is gained by going from daily to twice-daily (factor of 3.4) than
254 going from twice-daily to hourly (factor of 2.9), because of the temporal error correlation in the
255 transport model. The aspirational hi-res satellite configuration provides 2,221 pieces of information
256 on temporally invariant sources, corresponding to 85% of the flux patterns, which means that much
257 of the spatial variability in the $1.3 \times 1.3 \text{ km}^2$ emissions in the Barnett Shale is resolved.

258 Figure 6 further quantifies the importance of instrument precision and return frequency for the
259 GeoCARB pixel resolution of $2.7 \times 3.0 \text{ km}^2$. It shows the flux thresholds for a set of configurations
260 where the instrument precision is varied from 0 to 14 ppb and the return frequency is varied from 1
261 to 10 returns per day. We find that instrument precision is more important than return frequency for
262 increasing the information content from the observations.

263 In Case #2 we assume that the methane sources in individual pixels vary in time on an hourly
264 basis with no correlation from one hour to the next, making the problem generally underdetermined

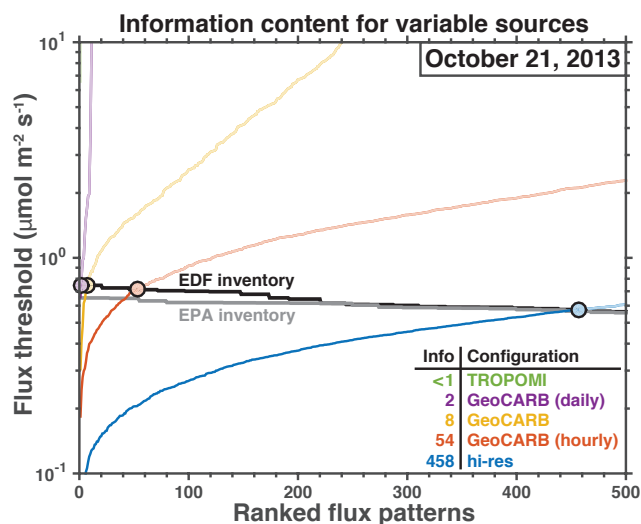


Fig. 7. Same as Fig. 5 but for temporally variable sources on October 21, 2013.

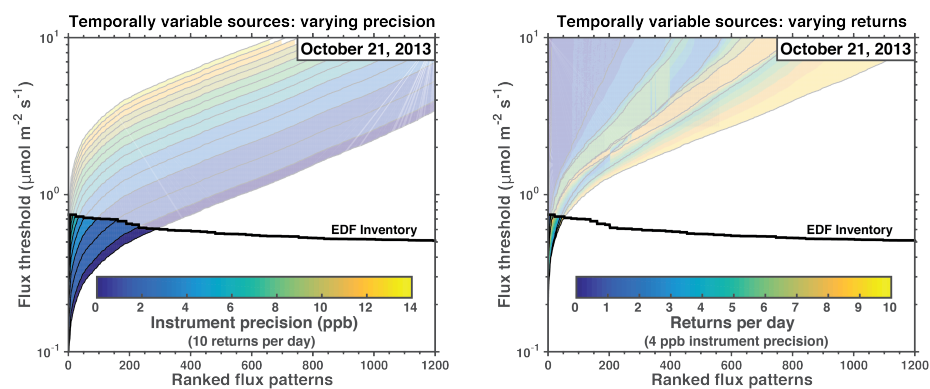


Fig. 8. Same as Fig. 6 but for temporally variable sources on October 21, 2013.



265 ($m < n$) for all satellite configurations. Here we aim to determine the ability of the satellite obser-
266 vations to quantify the hourly emissions over the spatial patterns defined by the eigenvectors of \mathcal{F}
267 and making no assumption as to the persistence of those emissions. We treat each day independently
268 and compute the eigenvalues of the Fisher information matrix for each day. Figure 7 shows the
269 flux thresholds for the five satellite configurations on a representative day. From Fig. 7, we see that
270 TROPOMI is unable to provide any information on hourly emissions in the Barnett Shale. The three
271 GeoCARB configurations provide 2–54 pieces of information. Fig. 8 evaluates the impact of sam-
272 pling frequency and instrument precision for the GeoCARB configurations. As with the temporally
273 invariant case, we find that instrument precision is more important for increasing the information
274 content. The aspirational “hi-res” configuration (shown in Fig. 7) is the only configuration that is
275 able to provide substantial information (458 pieces of information) on temporally variable emissions.

276 Figure 9 summarizes the findings from Figs. 6 and 8. It compares the information content \mathcal{I} from
277 configurations with $2.7 \times 3.0 \text{ km}^2$ spatial resolution (GeoCARB) as the instrument precision and
278 return frequency are varied from 0 to 14 ppb and 1 to 10 returns per day, respectively, for both tem-
279 porally variable and constant sources. Uncertainty on \mathcal{I} is estimated by randomly sampling e_i from
280 the ensemble of emission inventory eigenvalues and comparing to f_i in Eq. 8. For the temporally
281 invariant sources (Case #1), we find considerable increases in information content for instrument pre-
282 cisions better than 6 ppb (top left panel in Fig. 9) and an approximately linear relationship between
283 information content and return frequency (top right panel in Fig. 9). The satellite configurations
284 provide considerably less information for the temporally variable sources (Case #2). We find that
285 satellite configurations with an instrument precisions worse than 6 ppb provide no information on
286 temporally variable sources (bottom left panel in Fig. 9). As with the temporally invariant case, we
287 find an approximately linear relationship between information content and return frequency (bottom
288 right panel in Fig. 9). From this, we conclude that a GeoCARB-like instrument would greatly benefit
289 from having an instrument precision better than 6 ppb.

290 5 Conclusions

291 We conducted an observing system simulation experiment (OSSE) to evaluate the potential of dif-
292 ferent satellite observation systems for atmospheric methane to quantify methane emissions at kilo-
293 meter scale. This involved a 1-week WRF-STILT simulation of atmospheric methane columns with
294 $1.3 \times 1.3 \text{ km}^2$ spatial resolution over a $290 \times 235 \text{ km}^2$ domain (Barnett Shale of Northeast Texas)
295 to quantify the information content of different satellite instrument configurations for resolving the
296 kilometer-scale distribution of methane emissions within that domain. We evaluated the information
297 content of the different satellite observing systems through an eigenanalysis of the Fisher informa-
298 tion matrix \mathcal{F} , which characterizes the capability of an observing system independently of the form
299 of the prior information. The eigenvalues of \mathcal{F} define the emission flux thresholds for detection of

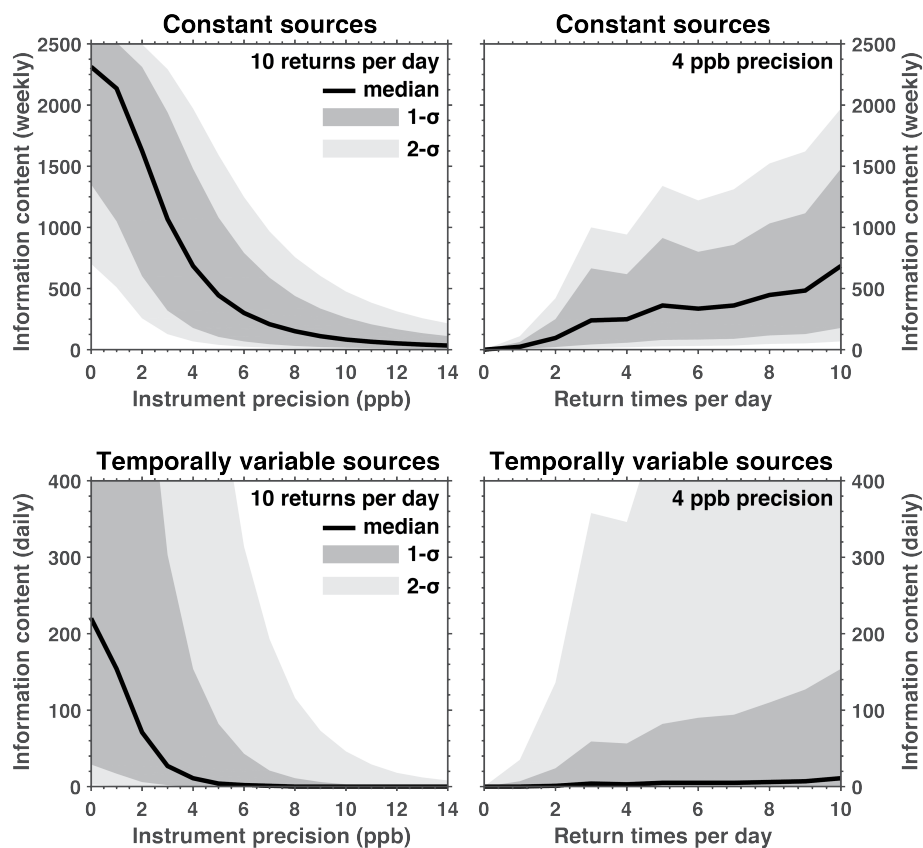


Fig. 9. Information content \mathcal{I} as a function of the instrument precision (left column) and the sampling frequency per day (right column) for a satellite with a pixel resolution of $2.7 \times 3.0 \text{ km}^2$. Top row is for Case #1 where the sources are assumed to be temporally invariant and bottom row is for Case #2 where the sources are temporally variable. Solid black line is the median information content. A 4 ppb model error is included, see Section 3. Uncertainty is from randomly sampling e_i from the eigenvalues of the EDF inventory.



300 emission patterns down to 1.3 km in scale as defined by the eigenvectors. Here we put these flux
301 thresholds in context of the high-resolution EDF emission inventory for the Barnett Shale to quantify
302 the information content from different satellite observing configurations. The same approach could
303 be readily used for different observation domains and different prior inventories.

304 We find from this analysis that the recently launched TROPOMI satellite instrument (low Earth
305 orbit, 7×7 km² pixels, daily return time, 11 ppb precision) should be able to constrain the mean
306 emissions in the Barnett Shale and provide some coarse-resolution information on the distribution
307 of emissions. The planned GeoCARB instrument (geostationary orbit, 2.7×3.0 km² pixels, twice-
308 daily return time, 4 ppb precision), will provide 50 times more information than TROPOMI. The
309 observing frequency of GeoCARB is still under discussion; we find that twice-daily observations
310 triple the information content relative to daily observations, while hourly observations allow another
311 tripling. The 4 ppb precision of GeoCARB is well adapted to the magnitude of methane sources;
312 we find that a precision larger than 6 ppb would considerably decrease the information content. An
313 aspirational “hi-res” instrument using attributes of currently proposed instruments (geostationary
314 orbit, 1.3×1.3 km² pixels, hourly return time, 1 ppb precision) can resolve much of the kilometer-
315 scale spatial distribution in the EDF inventory. This assumes that the emissions are constant in time
316 or that their temporal variability is known. Resolving hourly variable emissions at the kilometer-
317 scale will be very limited even with the aspirational “hi-res” instrument.

318 Appendix Computing the information content

319 We treat \mathcal{F} and \mathbf{B}^{-1} separately because it is computationally infeasible to compute the eigenval-
320 ues of the matrix product when we attempt to resolve hourly emissions as $n > 10^6$ and both \mathcal{F}
321 and \mathbf{B}^{-1} are $n \times n$ matrices. This separation of \mathcal{F} and \mathbf{B}^{-1} results in our estimate of \mathcal{I} likely be-
322 ing an upper bound on the information content. This follows from Bhatia (1997) who prove that
323 $\lambda(\mathbf{CD}) \prec_w \lambda^\downarrow(\mathbf{C}) \cdot \lambda^\downarrow(\mathbf{D})$, where \mathbf{C} and \mathbf{D} are Hermitian positive definite matrices, $\lambda^\downarrow(\mathbf{X})$ de-
324 notes the vector of eigenvalues of \mathbf{X} in decreasing order, \prec_w is the weak majorization preorder,
325 and $\mathbf{p} \cdot \mathbf{q} = (p_1 q_1, \dots, p_n q_n)$. Therefore, directly computing the eigenvalues of $\mathbf{B}^{1/2} \mathcal{F} \mathbf{B}^{1/2}$, as
326 Rodgers (2000) suggests for the Bayesian inference case with Gaussian errors, would likely yield
327 fewer eigenvalues larger than unity than our estimate.

328 In the case of temporally variable emissions, the system is generally underdetermined ($m < n$)
329 and we can use a singular value decomposition to efficiently compute the eigenvalues of \mathcal{F} . For an
330 $m \times n$ real matrix \mathbf{A} , the non-zero singular values of $\mathbf{A}^T \mathbf{A}$ and $\mathbf{A} \mathbf{A}^T$ are identical (see, for example,
331 Rodgers, 2000) but the dimensions of these two matrices are $n \times n$ and $m \times m$, respectively, and the
332 eigenvalues can be computed from the square root of the non-zero singular values. We can write
333 $\mathcal{F} = \hat{\mathbf{H}}^T \hat{\mathbf{H}}$ where $\hat{\mathbf{H}} = \mathbf{L}^{-1} \mathbf{H}$ is the pre-whitened Jacobian and \mathbf{L} is a lower triangular matrix from
334 a Cholesky decomposition of \mathbf{R} (such that $\mathbf{R} = \mathbf{L} \mathbf{L}^T$). Thus, the eigenvalues of \mathcal{F} can be obtained



335 by analysis of either $\hat{\mathbf{H}}^T \hat{\mathbf{H}}$ (an $n \times n$ matrix) or $\hat{\mathbf{H}} \hat{\mathbf{H}}^T$ (an $m \times m$ matrix). Analysis of $\hat{\mathbf{H}} \hat{\mathbf{H}}^T$ does
336 not yield the eigenvectors of \mathcal{F} .

337 *Acknowledgements.* This work was supported by the ExxonMobil Research and Engineering Company and
338 the US Department of Energy (DOE) Advanced Research Projects Agency – Energy (ARPA-E). A. J. Turner
339 is supported as a Miller Fellow with the Miller Institute for Basic Research in Science at UC Berkeley. This
340 research used the Savio computational cluster resource provided by the Berkeley Research Computing program
341 at the University of California, Berkeley (supported by the UC Berkeley Chancellor, Vice Chancellor for Re-
342 search, and Chief Information Officer). This research also used resources from the National Energy Research
343 Scientific Computing Center, which is supported by the Office of Science of the U.S. Department of Energy
344 under Contract No. DE-AC02-05CH11231. We also acknowledge high-performance computing support from
345 Cheyenne (doi:10.5065/D6RX99HX) provided by NCAR’s Computational and Information Systems Labora-
346 tory, sponsored by the National Science Foundation.



347 References

- 348 Alexe, M., Bergamaschi, P., Segers, A., Detmers, R., Butz, A., Hasekamp, O., Guerlet, S., Parker, R., Boesch,
349 H., Frankenberg, C., Scheepmaker, R. A., Dlugokencky, E., Sweeney, C., Wofsy, S. C., and Kort, E. A.:
350 Inverse modelling of CH₄ emissions for 2010–2011 using different satellite retrieval products from GOSAT
351 and SCIAMACHY, *Atmospheric Chemistry and Physics*, 15, 113–133, doi:10.5194/acp-15-113-2015, 2015.
- 352 Bergamaschi, P., Frankenberg, C., Meirink, J. F., Krol, M., Villani, M. G., Houweling, S., Dentener, F., Dlu-
353 gokencky, E. J., Miller, J. B., Gatti, L. V., Engel, A., and Levin, I.: Inverse modeling of global and re-
354 gional CH₄ emissions using SCIAMACHY satellite retrievals, *Journal of Geophysical Research*, 114, doi:
355 10.1029/2009jd012287, 2009.
- 356 Bergamaschi, P., Houweling, S., Segers, A., Krol, M., Frankenberg, C., Scheepmaker, R. A., Dlugokencky, E.,
357 Wofsy, S. C., Kort, E. A., Sweeney, C., Schuck, T., Brenninkmeijer, C., Chen, H., Beck, V., and Gerbig, C.:
358 Atmospheric CH₄ in the first decade of the 21st century: Inverse modeling analysis using SCIAMACHY
359 satellite retrievals and NOAA surface measurements, *Journal of Geophysical Research: Atmospheres*, 118,
360 7350–7369, doi:10.1002/jgrd.50480, 2013.
- 361 Bhatia, R.: *Matrix Analysis*, Graduate Texts in Mathematics, Springer, New York, 1997.
- 362 Bousserez, N., Henze, D. K., Rooney, B., Perkins, A., Wecht, K. J., Turner, A. J., Natraj, V., and Worden,
363 J. R.: Constraints on methane emissions in North America from future geostationary remote-sensing mea-
364 surements, *Atmospheric Chemistry and Physics*, 16, 6175–6190, doi:10.5194/acp-16-6175-2016, 2016.
- 365 Bovensmann, H., Buchwitz, M., Burrows, J. P., Reuter, M., Krings, T., Gerilowski, K., Schneising, O., Hey-
366 mann, J., Tretner, A., and Erzinger, J.: A remote sensing technique for global monitoring of power plant
367 CO₂ emissions from space and related applications, *Atmospheric Measurement Techniques*, 3, 781–811,
368 doi:10.5194/amt-3-781-2010, 2010.
- 369 Brandt, A. R., Heath, G. A., Kort, E. A., O’Sullivan, F., Petron, G., Jordaan, S. M., Tans, P., Wilcox, J.,
370 Gopstein, A. M., Arent, D., Wofsy, S., Brown, N. J., Bradley, R., Stucky, G. D., Eardley, D., and Harriss,
371 R.: Energy and environment. Methane leaks from North American natural gas systems, *Science*, 343, 733–5,
372 doi:10.1126/science.1247045, 2014.
- 373 Brasseur, G. P. and Jacob, D. J.: *Modeling of Atmospheric Chemistry*, Princeton University Press, Princeton,
374 NJ, 2017.
- 375 Buchwitz, M., Reuter, M., Schneising, O., Boesch, H., Guerlet, S., Dils, B., Aben, I., Armante, R., Bergamaschi,
376 P., Blumenstock, T., Bovensmann, H., Brunner, D., Buchmann, B., Burrows, J. P., Butz, A., Chdin, A.,
377 Chevallier, F., Crevoisier, C. D., Deutscher, N. M., Frankenberg, C., Hase, F., Hasekamp, O. P., Heymann,
378 J., Kaminski, T., Laeng, A., Lichtenberg, G., De Mazire, M., Nol, S., Notholt, J., Orphal, J., Popp, C.,
379 Parker, R., Scholze, M., Sussmann, R., Stiller, G. P., Warneke, T., Zehner, C., Bril, A., Crisp, D., Griffith,
380 D. W. T., Kuze, A., O’Dell, C., Oshchepkov, S., Sherlock, V., Suto, H., Wennberg, P., Wunch, D., Yokota,
381 T., and Yoshida, Y.: The Greenhouse Gas Climate Change Initiative (GHG-CCI): Comparison and quality
382 assessment of near-surface-sensitive satellite-derived CO₂ and CH₄ global data sets, *Remote Sensing of*
383 *Environment*, 162, 344–362, doi:10.1016/j.rse.2013.04.024, 2015.
- 384 Buchwitz, M., Schneising, O., Reuter, M., Heymann, J., Krautwurst, S., Bovensmann, H., Burrows, J. P.,
385 Boesch, H., Parker, R. J., Somkuti, P., Detmers, R. G., Hasekamp, O. P., Aben, I., Butz, A., Frankenberg,
386 C., and Turner, A. J.: Satellite-derived methane hotspot emission estimates using a fast data-driven method,



- 387 Atmospheric Chemistry and Physics, 17, 5751–5774, doi:10.5194/acp-17-5751-2017, 2017.
- 388 Butz, A., Galli, A., Hasekamp, O., Landgraf, J., Tol, P., and Aben, I.: TROPOMI aboard Sentinel-5 Precursor:
389 Prospective performance of CH₄ retrievals for aerosol and cirrus loaded atmospheres, Remote Sensing of
390 Environment, 120, 267–276, doi:10.1016/j.rse.2011.05.030, 2012.
- 391 Butz, A., Orphal, J., Checa-Garcia, R., Friedl-Vallon, F., von Clarmann, T., Bovensmann, H., Hasekamp, O.,
392 Landgraf, J., Knigge, T., Weise, D., Squali-Houssini, O., and Kemper, D.: Geostationary Emission Explorer
393 for Europe (G3E): mission concept and initial performance assessment, Atmospheric Measurement Tech-
394 niques, 8, 4719–4734, doi:10.5194/amt-8-4719-2015, 2015.
- 395 Candes, E. J. and Wakin, M. B.: An introduction to compressive sampling, IEEE Signal Processing Magazine,
396 25, 21–30, doi:10.1109/Msp.2007.914731, 2008.
- 397 Caulton, D. R., Shepson, P. B., Santoro, R. L., Sparks, J. P., Howarth, R. W., Ingraffea, A. R., Cambaliza,
398 M. O., Sweeney, C., Karion, A., Davis, K. J., Stirm, B. H., Montzka, S. A., and Miller, B. R.: Toward a
399 better understanding and quantification of methane emissions from shale gas development, Proc Natl Acad
400 Sci U S A, doi:10.1073/pnas.1316546111, 2014.
- 401 Conley, S., Franco, G., Faloona, I., Blake, D. R., Peischl, J., and Ryerson, T. B.: Methane emissions from
402 the 2015 Aliso Canyon blowout in Los Angeles, CA, Science, 351, 1317–20, doi:10.1126/science.aaf2348,
403 2016.
- 404 Cressot, C., Chevallier, F., Bousquet, P., Crevoisier, C., Dlugokencky, E. J., Fortems-Cheiney, A., Frankenberg,
405 C., Parker, R., Pison, I., Scheepmaker, R. A., Montzka, S. A., Krummel, P. B., Steele, L. P., and Langenfelds,
406 R. L.: On the consistency between global and regional methane emissions inferred from SCIAMACHY,
407 TANSO-FTS, IASI and surface measurements, Atmospheric Chemistry and Physics, 14, 577–592, doi:10.
408 5194/acp-14-577-2014, 2014.
- 409 Fishman, J., Iraci, L. T., Al-Saadi, J., Chance, K., Chavez, F., Chin, M., Coble, P., Davis, C., DiGiacomo, P. M.,
410 Edwards, D., Eldering, A., Goes, J., Herman, J., Hu, C., Jacob, D. J., Jordan, C., Kawa, S. R., Key, R., Liu,
411 X., Lohrenz, S., Mannino, A., Natraj, V., Neil, D., Neu, J., Newchurch, M., Pickering, K., Salisbury, J.,
412 Sosik, H., Subramaniam, A., Tzortziou, M., Wang, J., and Wang, M.: The United States’ Next Generation of
413 Atmospheric Composition and Coastal Ecosystem Measurements: NASA’s Geostationary Coastal and Air
414 Pollution Events (GEO-CAPE) Mission, Bulletin of the American Meteorological Society, 93, 1547–1566,
415 doi:10.1175/bams-d-11-00201.1, 2012.
- 416 Frankenberg, C., Meirink, J. F., van Weele, M., Platt, U., and Wagner, T.: Assessing methane emissions from
417 global space-borne observations, Science, 308, 1010–4, doi:10.1126/science.1106644, 2005.
- 418 Frankenberg, C., Thorpe, A. K., Thompson, D. R., Hulley, G., Kort, E. A., Vance, N., Borchardt, J., Krings, T.,
419 Gerilowski, K., Sweeney, C., Conley, S., Bue, B. D., Aubrey, A. D., Hook, S., and Green, R. O.: Airborne
420 methane remote measurements reveal heavy-tail flux distribution in Four Corners region, Proc Natl Acad Sci
421 U S A, 113, 9734–9, doi:10.1073/pnas.1605617113, 2016.
- 422 Fraser, A., Palmer, P. I., Feng, L., Boesch, H., Cogan, A., Parker, R., Dlugokencky, E. J., Fraser, P. J., Krummel,
423 P. B., Langenfelds, R. L., O’Doherty, S., Prinn, R. G., Steele, L. P., van der Schoot, M., and Weiss, R. F.:
424 Estimating regional methane surface fluxes: the relative importance of surface and GOSAT mole fraction
425 measurements, Atmospheric Chemistry and Physics, 13, 5697–5713, doi:10.5194/acp-13-5697-2013, 2013.
- 426 Houweling, S., Bergamaschi, P., Chevallier, F., Heimann, M., Kaminski, T., Krol, M., Michalak, A. M., and Pa-



- 427 tra, P.: Global inverse modeling of CH₄ sources and sinks: An overview of methods, *Atmospheric Chemistry*
428 *and Physics Discussions*, pp. 1–30, doi:10.5194/acp-2016-572, 2016.
- 429 Hu, H., Hasekamp, O., Butz, A., Galli, A., Landgraf, J., Aan de Brugh, J., Borsdorff, T., Scheepmaker, R.,
430 and Aben, I.: The operational methane retrieval algorithm for TROPOMI, *Atmospheric Measurement Tech-*
431 *niques*, 9, 5423–5440, doi:10.5194/amt-9-5423-2016, 2016.
- 432 Jacob, D. J., Turner, A. J., Maasakkers, J. D., Sheng, J., Sun, K., Liu, X., Chance, K., Aben, I., McKeever, J.,
433 and Frankenberg, C.: Satellite observations of atmospheric methane and their value for quantifying methane
434 emissions, *Atmospheric Chemistry and Physics*, 16, 14 371–14 396, doi:10.5194/acp-16-14371-2016, 2016.
- 435 Karion, A., Sweeney, C., Ptron, G., Frost, G., Michael Hardesty, R., Kofler, J., Miller, B. R., Newberger, T.,
436 Wolter, S., Banta, R., Brewer, A., Dlugokencky, E., Lang, P., Montzka, S. A., Schnell, R., Tans, P., Trainer,
437 M., Zamora, R., and Conley, S.: Methane emissions estimate from airborne measurements over a western
438 United States natural gas field, *Geophysical Research Letters*, 40, 4393–4397, doi:10.1002/grl.50811, 2013.
- 439 Karion, A., Sweeney, C., Kort, E. A., Shepson, P. B., Brewer, A., Cambaliza, M., Conley, S. A., Davis, K.,
440 Deng, A., Hardesty, M., Herndon, S. C., Lauvaux, T., Lavoie, T., Lyon, D., Newberger, T., Petron, G., Rella,
441 C., Smith, M., Wolter, S., Yacovitch, T. I., and Tans, P.: Aircraft-Based Estimate of Total Methane Emissions
442 from the Barnett Shale Region, *Environ Sci Technol*, 49, 8124–31, doi:10.1021/acs.est.5b00217, 2015.
- 443 Kirschke, S., Bousquet, P., Ciais, P., Saunois, M., Canadell, J. G., Dlugokencky, E. J., Bergamaschi, P.,
444 Bergmann, D., Blake, D. R., Bruhwiler, L., Cameron-Smith, P., Castaldi, S., Chevallier, F., Feng, L., Fraser,
445 A., Heimann, M., Hodson, E. L., Houweling, S., Josse, B., Fraser, P. J., Krummel, P. B., Lamarque, J.-F.,
446 Langenfelds, R. L., Le Qur, C., Naik, V., O’Doherty, S., Palmer, P. I., Pison, I., Plummer, D., Poulter, B.,
447 Prinn, R. G., Rigby, M., Ringeval, B., Santini, M., Schmidt, M., Shindell, D. T., Simpson, I. J., Spahni, R.,
448 Steele, L. P., Strode, S. A., Sudo, K., Szopa, S., van der Werf, G. R., Voulgarakis, A., van Weele, M., Weiss,
449 R. F., Williams, J. E., and Zeng, G.: Three decades of global methane sources and sinks, *Nature Geoscience*,
450 6, 813–823, doi:10.1038/ngeo1955, 2013.
- 451 Kort, E. A., Frankenberg, C., Costigan, K. R., Lindenmaier, R., Dubey, M. K., and Wunch, D.: Four
452 corners: The largest US methane anomaly viewed from space, *Geophysical Research Letters*, 41, doi:
453 10.1002/2014gl061503, 2014.
- 454 Kuze, A., Suto, H., Nakajima, M., and Hamazaki, T.: Thermal and near infrared sensor for carbon observation
455 Fourier-transform spectrometer on the Greenhouse Gases Observing Satellite for greenhouse gases monitor-
456 ing, *Appl Opt*, 48, 6716–33, doi:10.1364/AO.48.006716, 2009.
- 457 Kuze, A., Suto, H., Shiomi, K., Kawakami, S., Tanaka, M., Ueda, Y., Deguchi, A., Yoshida, J., Yamamoto,
458 Y., Kataoka, F., Taylor, T. E., and Buijs, H. L.: Update on GOSAT TANSO-FTS performance, operations,
459 and data products after more than 6 years in space, *Atmospheric Measurement Techniques*, 9, 2445–2461,
460 doi:10.5194/amt-9-2445-2016, 2016.
- 461 Lavoie, T. N., Shepson, P. B., Cambaliza, M. O., Stirm, B. H., Karion, A., Sweeney, C., Yacovitch, T. I.,
462 Herndon, S. C., Lan, X., and Lyon, D.: Aircraft-Based Measurements of Point Source Methane Emissions
463 in the Barnett Shale Basin, *Environ Sci Technol*, 49, 7904–13, doi:10.1021/acs.est.5b00410, 2015.
- 464 Lin, J. C., Gerbig, C., Wofsy, S. C., Andrews, A. E., Daube, B. C., Davis, K. J., and Grainger, C. A.: A near-
465 field tool for simulating the upstream influence of atmospheric observations: The Stochastic Time-Inverted
466 Lagrangian Transport (STILT) model, *Journal of Geophysical Research-Atmospheres*, 108, ACH 2–1–ACH



- 467 2–17, doi:10.1029/2002jd003161, 2003.
- 468 Lyon, D. R., Zavala-Araiza, D., Alvarez, R. A., Harriss, R., Palacios, V., Lan, X., Talbot, R., Lavoie, T.,
469 Shepson, P., Yacovitch, T. I., Herndon, S. C., Marchese, A. J., Zimmerle, D., Robinson, A. L., and Hamburg,
470 S. P.: Constructing a Spatially Resolved Methane Emission Inventory for the Barnett Shale Region, Environ
471 Sci Technol, 49, 8147–57, doi:10.1021/es506359c, 2015.
- 472 Maasackers, J. D., Jacob, D. J., Sulprizio, M. P., Turner, A. J., Weitz, M., Wirth, T., Hight, C., DeFigueiredo,
473 M., Desai, M., Schmeltz, R., Hockstad, L., Bloom, A. A., Bowman, K. W., Jeong, S., and Fischer, M. L.:
474 Gridded National Inventory of U.S. Methane Emissions, Environ Sci Technol, 50, 13 123–13 133, doi:10.
475 1021/acs.est.6b02878, 2016.
- 476 Miller, S. M., Wofsy, S. C., Michalak, A. M., Kort, E. A., Andrews, A. E., Biraud, S. C., Dlugokencky,
477 E. J., Eluszkiewicz, J., Fischer, M. L., Janssens-Maenhout, G., Miller, B. R., Miller, J. B., Montzka, S. A.,
478 Nehrkorn, T., and Sweeney, C.: Anthropogenic emissions of methane in the United States, Proc Natl Acad
479 Sci U S A, 110, 20018–22, doi:10.1073/pnas.1314392110, 2013.
- 480 Monteil, G., Houweling, S., Butz, A., Guerlet, S., Schepers, D., Hasekamp, O., Frankenberg, C., Scheep-
481 maker, R., Aben, I., and Rckmann, T.: Comparison of CH₄ inversions based on 15 months of GOSAT
482 and SCIAMACHY observations, Journal of Geophysical Research: Atmospheres, 118, 11,807–11,823, doi:
483 10.1002/2013jd019760, 2013.
- 484 O'Brien, D. M., Polonsky, I. N., Utembe, S. R., and Rayner, P. J.: Potential of a geostationary geoCARB
485 mission to estimate surface emissions of CO₂, CH₄ and CO in a polluted urban environment: case study
486 Shanghai, Atmospheric Measurement Techniques, 9, 4633–4654, doi:10.5194/amt-9-4633-2016, 2016.
- 487 O'Dell, C. W., Connor, B., Bsch, H., O'Brien, D., Frankenberg, C., Castano, R., Christi, M., Eldering, D.,
488 Fisher, B., Gunson, M., McDuffie, J., Miller, C. E., Natraj, V., Oyafuso, F., Polonsky, I., Smyth, M., Taylor,
489 T., Toon, G. C., Wennberg, P. O., and Wunch, D.: The ACOS CO₂ retrieval algorithm Part 1: Description
490 and validation against synthetic observations, Atmospheric Measurement Techniques, 5, 99–121, doi:10.
491 5194/amt-5-99-2012, 2012.
- 492 Peischl, J., Ryerson, T. B., Aikin, K. C., de Gouw, J. A., Gilman, J. B., Holloway, J. S., Lerner, B. M., Nadkarni,
493 R., Neuman, J. A., Nowak, J. B., Trainer, M., Warneke, C., and Parrish, D. D.: Quantifying atmospheric
494 methane emissions from the Haynesville, Fayetteville, and northeastern Marcellus shale gas production re-
495 gions, Journal of Geophysical Research-Atmospheres, 120, 2119–2139, doi:10.1002/2014JD022697, 2015.
- 496 Peischl, J., Karion, A., Sweeney, C., Kort, E. A., Smith, M. L., Brandt, A. R., Yeskoo, T., Aikin, K. C., Conley,
497 S. A., Gvakharia, A., Trainer, M., Wolter, S., and Ryerson, T. B.: Quantifying atmospheric methane emis-
498 sions from oil and natural gas production in the Bakken shale region of North Dakota, Journal of Geophysical
499 Research: Atmospheres, 121, 6101–6111, doi:10.1002/2015jd024631, 2016.
- 500 Polonsky, I. N., O'Brien, D. M., Kumer, J. B., and O'Dell, C. W.: Performance of a geostationary mission, geo-
501 CARB, to measure CO₂, CH₄ and CO column-averaged concentrations, Atmospheric Measurement Tech-
502 niques, 7, 959–981, doi:10.5194/amt-7-959-2014, 2014.
- 503 Rayner, P. J., Utembe, S. R., and Crowell, S.: Constraining regional greenhouse gas emissions using geostation-
504 ary concentration measurements: a theoretical study, Atmospheric Measurement Techniques, 7, 3285–3293,
505 doi:10.5194/amt-7-3285-2014, 2014.
- 506 Rodgers, C. D.: Inverse Methods for Atmospheric Sounding, World Scientific, Singapore, 2000.



- 507 Saunois, M., Bousquet, P., Poulter, B., Peregon, A., Ciais, P., Canadell, J. G., Dlugokencky, E. J., Etiope, G.,
508 Bastviken, D., Houweling, S., Janssens-Maenhout, G., Tubiello, F. N., Castaldi, S., Jackson, R. B., Alexe,
509 M., Arora, V. K., Beerling, D. J., Bergamaschi, P., Blake, D. R., Brailsford, G., Brovkin, V., Bruhwiler, L.,
510 Crevoisier, C., Crill, P., Covey, K., Curry, C., Frankenberg, C., Gedney, N., Hglund-Isaksson, L., Ishizawa,
511 M., Ito, A., Joos, F., Kim, H.-S., Kleinen, T., Krummel, P., Lamarque, J.-F., Langenfelds, R., Locatelli,
512 R., Machida, T., Maksyutov, S., McDonald, K. C., Marshall, J., Melton, J. R., Morino, I., Naik, V., amp,
513 apos, Doherty, S., Parmentier, F.-J. W., Patra, P. K., Peng, C., Peng, S., Peters, G. P., Pison, I., Prigent,
514 C., Prinn, R., Ramonet, M., Riley, W. J., Saito, M., Santini, M., Schroeder, R., Simpson, I. J., Spahni, R.,
515 Steele, P., Takizawa, A., Thornton, B. F., Tian, H., Tohjima, Y., Viovy, N., Voulgarakis, A., van Weele, M.,
516 van der Werf, G. R., Weiss, R., Wiedinmyer, C., Wilton, D. J., Wiltshire, A., Worthly, D., Wunch, D., Xu,
517 X., Yoshida, Y., Zhang, B., Zhang, Z., and Zhu, Q.: The global methane budget 20002012, *Earth System*
518 *Science Data*, 8, 697–751, doi:10.5194/essd-8-697-2016, 2016.
- 519 Sheng, J.-X., Jacob, D. J., Turner, A. J., Maasackers, J. D., Sulprizio, M. P., Bloom, A. A., Andrews, A. E.,
520 and Wunch, D.: High-resolution inversion of methane emissions in the Southeast US using SEAC⁴RS air-
521 craft observations of atmospheric methane: anthropogenic and wetland sources, *Atmospheric Chemistry and*
522 *Physics Discussions*, pp. 1–17, doi:10.5194/acp-2017-1151, 2017.
- 523 Sheng, J.-X., Jacob, D. J., Turner, A. J., Maasackers, J. D., Benmergui, J., Bloom, A. A., Arndt, C., Gautam, R.,
524 Zavala-Araiza, D., Boesch, H., and Parker, R. J.: 2010–2015 methane trends over Canada, the United States,
525 and Mexico observed by the GOSAT satellite: contributions from different source sectors, *Atmospheric*
526 *Chemistry and Physics Discussions*, pp. 1–18, doi:10.5194/acp-2017-1110, 2018.
- 527 Skamarock, W. C., Klemp, J. B., Dudhia, J., Gill, D. O., Barker, D. M., Duda, M. G., Huang, X.-Y., Wang, W.,
528 and Powers, J. G.: A Description of the Advanced Research WRF Version 3, Tech. rep., National Center for
529 Atmospheric Research, doi:10.5065/D68S4MVH, 2008.
- 530 Tan, Z., Zhuang, Q., Henze, D. K., Frankenberg, C., Dlugokencky, E., Sweeney, C., Turner, A. J., Sasakawa, M.,
531 and Machida, T.: Inverse modeling of pan-Arctic methane emissions at high spatial resolution: what can we
532 learn from assimilating satellite retrievals and using different process-based wetland and lake biogeochemical
533 models?, *Atmospheric Chemistry and Physics*, 16, 12 649–12 666, doi:10.5194/acp-16-12649-2016, 2016.
- 534 Tarantola, A.: *Inverse Problem Theory and Methods for Model Parameter Estimation*, Society for Industrial
535 and Applied Mathematics, Philadelphia, PA, USA, 2004.
- 536 Turner, A. J. and Jacob, D. J.: Balancing aggregation and smoothing errors in inverse models, *Atmospheric*
537 *Chemistry and Physics*, 15, 7039–7048, doi:10.5194/acp-15-7039-2015, 2015.
- 538 Turner, A. J., Jacob, D. J., Wecht, K. J., Maasackers, J. D., Lundgren, E., Andrews, A. E., Biraud, S. C.,
539 Boesch, H., Bowman, K. W., Deutscher, N. M., Dubey, M. K., Griffith, D. W. T., Hase, F., Kuze, A.,
540 Notholt, J., Ohyama, H., Parker, R., Payne, V. H., Sussmann, R., Sweeney, C., Velazco, V. A., Warneke,
541 T., Wennberg, P. O., and Wunch, D.: Estimating global and North American methane emissions with high
542 spatial resolution using GOSAT satellite data, *Atmospheric Chemistry and Physics*, 15, 7049–7069, doi:
543 10.5194/acp-15-7049-2015, 2015.
- 544 Turner, A. J., Jacob, D. J., Benmergui, J., Wofsy, S. C., Maasackers, J. D., Butz, A., Hasekamp, O., and Biraud,
545 S. C.: A large increase in U.S. methane emissions over the past decade inferred from satellite data and surface
546 observations, *Geophysical Research Letters*, pp. 2218–2224, doi:10.1002/2016gl067987, 2016a.



- 547 Turner, A. J., Shusterman, A. A., McDonald, B. C., Teige, V., Harley, R. A., and Cohen, R. C.: Network
548 design for quantifying urban CO₂ emissions: assessing trade-offs between precision and network density,
549 Atmospheric Chemistry and Physics, 16, 13465–13475, doi:10.5194/acp-16-13465-2016, 2016b.
- 550 Turner, A. J., Frankenberg, C., Wennberg, P. O., and Jacob, D. J.: Ambiguity in the causes for decadal trends
551 in atmospheric methane and hydroxyl, Proc Natl Acad Sci U S A, 114, 5367–5372, doi:10.1073/pnas.
552 1616020114, 2017.
- 553 Veefkind, J. P., Aben, I., McMullan, K., Frster, H., de Vries, J., Otter, G., Claas, J., Eskes, H. J., de Haan, J. F.,
554 Kleipool, Q., van Weele, M., Hasekamp, O., Hoogeveen, R., Landgraf, J., Snel, R., Tol, P., Ingmann, P.,
555 Voors, R., Kruizinga, B., Vink, R., Visser, H., and Levelt, P. F.: TROPOMI on the ESA Sentinel-5 Precursor:
556 A GMES mission for global observations of the atmospheric composition for climate, air quality and ozone
557 layer applications, Remote Sensing of Environment, 120, 70–83, doi:10.1016/j.rse.2011.09.027, 2012.
- 558 Wecht, K. J., Jacob, D. J., Frankenberg, C., Jiang, Z., and Blake, D. R.: Mapping of North American methane
559 emissions with high spatial resolution by inversion of SCIAMACHY satellite data, Journal of Geophysical
560 Research: Atmospheres, 119, 7741–7756, doi:10.1002/2014jd021551, 2014a.
- 561 Wecht, K. J., Jacob, D. J., Sulprizio, M. P., Santoni, G. W., Wofsy, S. C., Parker, R., Bsch, H., and Worden, J.:
562 Spatially resolving methane emissions in California: constraints from the CalNex aircraft campaign and from
563 present (GOSAT, TES) and future (TROPOMI, geostationary) satellite observations, Atmospheric Chemistry
564 and Physics, 14, 8173–8184, doi:10.5194/acp-14-8173-2014, 2014b.
- 565 Worden, J. R., Turner, A. J., Bloom, A., Kulawik, S. S., Liu, J., Lee, M., Weidner, R., Bowman, K., Frankenberg,
566 C., Parker, R., and Payne, V. H.: Quantifying lower tropospheric methane concentrations using GOSAT
567 near-IR and TES thermal IR measurements, Atmospheric Measurement Techniques, 8, 3433–3445, doi:
568 10.5194/amt-8-3433-2015, 2015.
- 569 Xi, X., Natraj, V., Shia, R. L., Luo, M., Zhang, Q., Newman, S., Sander, S. P., and Yung, Y. L.: Simulated
570 retrievals for the remote sensing of CO₂, CH₄, CO, and H₂O from geostationary orbit, Atmospheric Mea-
571 surement Techniques, 8, 4817–4830, doi:10.5194/amt-8-4817-2015, 2015.
- 572 Zavala-Araiza, D., Lyon, D. R., Alvarez, R. A., Davis, K. J., Harriss, R., Herndon, S. C., Karion, A., Kort,
573 E. A., Lamb, B. K., Lan, X., Marchese, A. J., Pacala, S. W., Robinson, A. L., Shepson, P. B., Sweeney,
574 C., Talbot, R., Townsend-Small, A., Yacovitch, T. I., Zimmerle, D. J., and Hamburg, S. P.: Reconciling
575 divergent estimates of oil and gas methane emissions, Proc Natl Acad Sci U S A, 112, 15597–602, doi:
576 10.1073/pnas.1522126112, 2015.